PHYSICAL REVIEW B **92**, 205133 (2015)

Intrinsic large gap quantum anomalous Hall insulators in LaX(X = Br, Cl, I)

Kapildeb Dolui, Sujay Ray, and Tanmoy Das
Department of Physics, Indian Institute of Science, Bangalore 560012, India

(Received 4 March 2015; revised manuscript received 8 May 2015; published 30 November 2015)

We report a theoretical prediction of a new class of bulk and intrinsic quantum anomalous Hall (QAH) insulators LaX (X=Br, Cl, and I) via relativistic first-principles calculations. We find that these systems are innate long-ranged ferromagnets which, with the help of intrinsic spin-orbit coupling, become QAH insulators. A low-energy multiband tight-binding model is developed to understand the origin of the QAH effect. Finally, integer Chern number is obtained via Berry phase computation for each two-dimensional plane. These materials have the added benefit of a sizable band gap of as large as ∼25 meV, with the flexibility of enhancing it to above 75 meV via strain engineering. The synthesis of LaX materials will provide the impurity-free single crystals and thin-film QAH insulators for versatile experiments and functionalities.

DOI: 10.1103/PhysRevB.92.205133 PACS number(s): 73.43.Cd, 73.23.−b, 75.10.−b, 75.50.Dd

I. INTRODUCTION

The discovery of the quantum Hall effect in 1980 (Ref. [1]) has widely encouraged the study of topological invariants in solid-state systems [2–7]. This has also contributed to the inception of many new physical concepts such as Thouless–Kohmoto–Nightingale–en Nijs (TKNN) invariants [2], composite fermions [8], and also raised the hope for the realization of many non-Abelian "particles" in condensed matter setups [5,6]. Subsequently, quantum spin-Hall (QSH) [9] and quantum anomalous Hall (QAH) [10,11] states were realized in which Hall current arises in the absence of external magnetic field. In both cases transverse spin current arises from the chiral spin-orbit entanglement with and without time-reversal symmetry, respectively. In these two subclasses, density functional theory (DFT) has taken the preceding role in predicting suitable materials, which were followed by experimental realizations.

The fascinating interplay between topological, magnetic, and transport properties of QAH effects has tremendous scientific and technological interests. Therefore the discovery of single-crystal QAH insulators with intrinsic long-range magnetization is considered imperative. Most of the search for QAH materials have so far been within the two-dimensional (2D) QSH or thin films of topological insulators. The idea here is to suppress one of their chiral spin currents by inducing a ferromagnetic (FM) state through impurity, doping, or proximity effect. This guideline has led to the predictions of a variety of materials within the magnetically doped graphene [12], QSH systems [13], thin films of topological insulators [14], quantum well states of Weyl semimetal $HgCr_2Se_4$ [15], and related materials (a comprehensive list of the predicted QAH materials is provided in Table I). Thin films of topological insulators are synthesized to date to exhibit a QAH effect with magnetic impurities [10,11]. However, so far there is no single crystal with innate magnetic order and spin-orbit coupling (SOC) known to be a QAH insulator.

We begin by considering the vast possibility of magnetic materials with strong SOC, and narrow down the list by eliminating the choices via crystal structure selection, absence of continuous magnetic transition, or impurity-prone lattice, etc. By using density functional theory (DFT) calculations, we find that the FM LaX (X=Br, Cl, and I) is a layered material class which exhibits band crossing between different orbitals and opposite spins at a momenta contour near the Fermi level without SOC [16]. As SOC is switched on, the "inverted" insulating band gap opens in LaBr, LaCl, and LaI, but not in LaF, endowing the former systems into the uncharted territory of intrinsic QAH insulators. To understand and characterize these properties, we have also formulated a realistic tight-binding model and estimated the QAH index via Berry curvature computation. LaBr and LaCl are also found to be flexible for enhancing their band gap via small strain. Much like how Bi- and Sb-based binary topological insulators provided the breakthrough for the discovery and predictions of many related materials and their ternary and quaternary variants, our prediction provides a guiding principle for manipulating and expanding the "bulk" and intrinsic QAH insulator classes in related materials.

The reminder of this article is organized as follows. In Sec. II, we describe the materials selection process for the QAH insulators. The corresponding first-principles band structure calculation for LaX family is performed in Sec. III A. Then we develop a material-specific two-band tight-binding model for LaX with SOC and FM order in Sec. III B. The Berry phase and Chern number calculations are presented in Sec. IV A. We have also demonstrated the presence of edge states in Sec. IV B. Strain enhancement of the bulk gap is shown in Sec. V. Finally, we conclude in Sec. VI. In Appendix A, we present the details of the band progression from the paramagnetic state to the FM state with and without SOC. The full derivation of the tight-binding model is provided in Appendix B. A list of prior predicted and experimentally realized materials with the corresponding tuning parameter and band gap is created in Table I.

II. MATERIALS SELECTION

Candidate materials for bulk QAH insulators may be sought in compounds where (1) magnetism and SOC can be intrinsically present; (2) the magnetic transition is continuous with temperature, or otherwise the magnetic interactions would often not be long ranged; (3) the lattice structure should be less symmetric which has higher propensity towards band inversion [7]; and (4) single-crystal growth would be feasible with a clear surface state, where dopant or impurity scattering

TABLE I. List of predicted QAH systems with types of tuning and maximum band-gap estimation. For the second last two systems, the band gap depends on the tight-binding parameter values, and the realistic values are not known. The chosen family of materials are representative, and there can be more materials in these families, but the band gap is lesser.

Material	Type of tuning	Band gap(meV)	Reference(s)
Graphene	Sc, Mn, Fe, Cu adatoms	2.5, 4.5, 5.5, 7.0	[17] and [18]
	$BiFeO_3$ AFM insulator (proximity effect)	1.1 (4 with strain)	[12]
	5*d* transition metals (Hf, Ta, W, Re, Os, Ir, Pt) doping and applied electric field	20–80	[19]
Silicene	3*d* transition-metal absorbants	$\leqslant 30$	[20]
	Co doping	<1	[21]
	Applied electric field	$\sim 1e^{-3}$	[22]
Bi_2Te_3, Bi_2Se_3, Sb_2Te_3 (thin film, QW)	Cr, Fe doping	$\leqslant 50$	[14,23,24]
FM insulators (MnSe, MnTe, EuS)	Heavy metals (Bi, Pb, Hg etc.) substitution	1–142	[25]
FM insulators in nGdN/ nEuO/ SrO heterostructure	Heterostructure engineering	3–30	[26]
2D Organic topological insulators	Mn doping	9.5	[27]
InSb-based (*p-n* junction QW)	Mn doping	5	[28]
HgTe QW	Mn doping	$\leqslant 1e^{-3}$	[15]
$HgCr_2Se_4$	Thin film and QW	$\leqslant 1e^{-3}$	[13]
Double perovskites (Sr_2FeMoO_6, Ba_2FeReO_4, Sr_2CrWO_6, $La_2MnIrO_4/LaAlO_3$)	Heterostructure	0.1–26	[29] and [30]
Oxides ($LaNiO_3$, $SrTiO_2/SrIrO_3$, $Na_2Ir_2O_7$)	Heterostructure		[31–33]
Topological crystalline insulator	Thin-film and FM doping		[34]
LaX ($X =$ Cl, Br, I)	Intrinsic	10–30 (40–75 with strain)	Present work

can be made sufficiently small to achieve large values of transport properties.

Simple candidates may include *d*-electron ferromagnets in the heavy-element compounds, or intercalated with heavy elements for sufficiently large SOC. But these systems often have a cubic or tetragonal lattice, and in some cases, lack inversion symmetry, which sometimes reduces the band inversion strength [7]. A similar complication arises in simple *d*-electron antiferromagnets in which, moreover, the magnetic transitions are sometimes not continuous. In addition, many of these systems suffer from the problems of impurity and low transport properties.

More promising candidates can be expected within the actinide and lanthanide compounds. Actinides have a larger SOC strength. But due to the larger bandwidth of $5f$ states, the interaction strength decreases and they often escape magnetism. More importantly, radioactive materials suffer from radiation-induced defects. We then consider lanthanide-based rare-earth elements. Their low-energy spectrum remains poised between the d and f electronic configurations, which makes them versatile for commencing diverse materials properties. Among the rare-earth elements, lanthanum (La) provides the common element for materials with properties as diverse as half-Huesler topological insulators [35,36], colossal magnetoresistance [37], metal-insulator transition [38], as well as high-temperature superconductivity [39]. Therefore, La is a good candidate element to search for a large gap intrinsic QAH effect.

For the anion element, we consider halogen elements because of their high electronegativity, which enables strong chemical bonding with La cations. Furthermore, halogen elements form very weak bonds within the diatonic (X_2) element, raising the possibility for obtaining layered systems with topological consequences. Our search by DFT calculations indeed yielded stable compounds LaX (X=Br, Cl, and I), which belong to the rhombohedral crystal structure with the space group $R\bar{3}m$ and point group D^5_{3d}. As shown in Fig. 1(a), the structure is characterized by a sequence of triangular network layers composed of La and X atoms. Each bilayer has two inequivalent La atoms (denoted by A and B layers) arranged in patterns as demonstrated in Fig. 1(b). All such bilayers are related to each other by inversion symmetry along the c axis, and the interbilayer interaction arises from the weak van der Waals interaction and is thus considerably small.

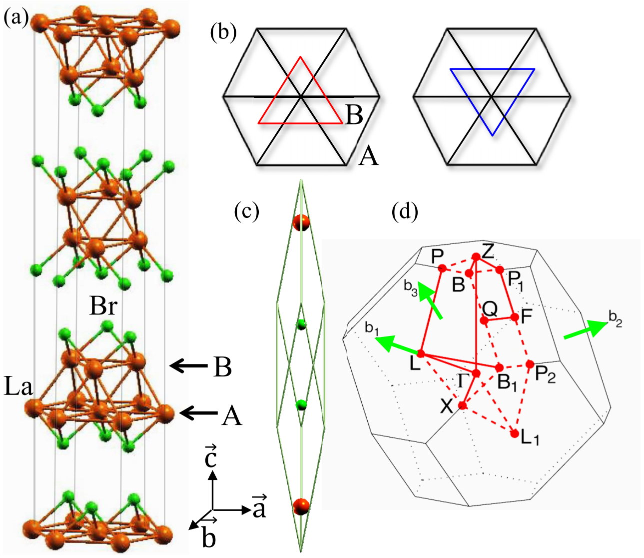

FIG. 1. (Color online) (a) Crystal structure of LaBr, with two inequivalent La atoms forming a bilayer, defined by a hexagonal layer with a triangle layer on its top or bottom plane, respectively. (b) Top view of two bilayers. The middle bilayer in (a) is same as other bilayers, but shifted in the *a*-*b* plane. (c) Primitive rhombohedral unit cell of LaBr. (d) Brillouin zone with space group of $R\bar{3}m$.

III. BAND STRUCTURE CALCULATIONS

A. First-principles calculation

Electronic structure calculations are carried out using DFT within the generalized gradient approximation (GGA) [40] as implemented within the VASP package [41]. Projected augmented-wave (PAW) [42] pseudopotentials are used to describe core electrons. The GGA+U method is used to deal with the strong correlations in these materials with the standard value of $U = 8$ eV on the correlated La $-$ 5d orbitals [43]. We have also explored a large range of U=0–8 eV, and the results remain characteristically the same. Moreover, the band structure is reproduced with other functionals including the local density approximation (LDA) + U, the van der Waals (vdW)-density functional (DF) [optB86b-vdW functional] method [44], and the hybrid functional HSE06 [45]. The conjugate gradient method is used to obtain relaxed geometries. Both atomic positions and cell parameters are allowed to relax, until the forces on each atom are less than 1 meV/Å. The optimized lattice vectors and atomic positions are listed in Ref. [46]. The kinetic energy cutoff of 650 eV and a k-mesh grid of $8 \times 8 \times 8$ are used in the self-consistent calculations. In order to analyze the stability of lattice dynamics, force constants are calculated for a $2 \times 2 \times 2$ supercell within the framework of density functional perturbation theory. Subsequently, the phonon dispersions are calculated using the PHONOPY package [47]. The formation enthalpy of LaX compound is calculated as $H_{\mathrm{f}}^{\mathrm{DFT}} = \mathrm{E}_{\mathrm{tot}}(\mathrm{La}X)–\mathrm{E}_{\mathrm{tot}}(\mathrm{La})–\mathrm{E}_{\mathrm{tot}}(X)$, where $\mathrm{E}_{\mathrm{tot}}(\mathrm{La}X)$, $\mathrm{E}_{\mathrm{tot}}(\mathrm{La})$, and $\mathrm{E}_{\mathrm{tot}}(X)$ are the total energy per formula unit of LaX, La, and X, respectively, in their bulk form. Both the phonon dispersion and formation energy show that LaX compounds are stable. Finally, given the valency of La ion being 3, the natural compound to expect is LaX_3 [43]. Therefore relative stabilities of the multiphase system are analyzed by comparing their formation enthalpies. Here the formation enthalpy of LaX is found to differ only slightly from that of LaX_3, and thus the former sample can also be grown easily. See Ref. [46] for further details of the DFT calculation and the results with various functionals, different values of U, 2D band plots, and others.

Both with and without SOC, the FM order is found to be the stable ground state for all the present systems, with a magnetic moment of $m = 0.8\mu_B$ per La atom. The FM order, oriented perpendicular to the La layers, is mediated by direct exchange interactions. The total energy of the FM ground states is lower by 0.22 and 0.21 eV/unit cells than the corresponding nonmagnetic and antiferromagnetic states, respectively.

The band progression of the representative compound LaBr is shown in Fig. 2 (also see Fig. 6). La has the 4f electrons fully filled, and its local moment is not often accessible to the conduction electrons. The magnetic moment arises in the half-filled 5d shell as a result of large Hund's rule coupling. The local crystal field environment of the La ion leads to large splitting between the e_g and t_g states, and two partially filled e_g orbitals osculate the Fermi level, with an overlapping semimetalliclike band structure.

In the FM state, strong Hund's coupling leads to spin splittings of the $d_{x^2-y^2}$ and d_{z^2} orbitals. The two majority and minority spin states from two different orbitals cross each other across the Fermi level, creating an inverted band structure near E_{F}, as shown in Fig. 2(a) for several high-symmetric directions. Such a contour of the inverted band crossing is often called Dirac line nodes, or a nodal Weyl ring [16,48–50]. The average FM exchange splitting can be estimated as $\Delta E = 2Jm = 0.8$ eV. By the value of the exchange coupling $J = 0.5$ eV, we can estimate the FM Curie temperature to be as high as 390 K.

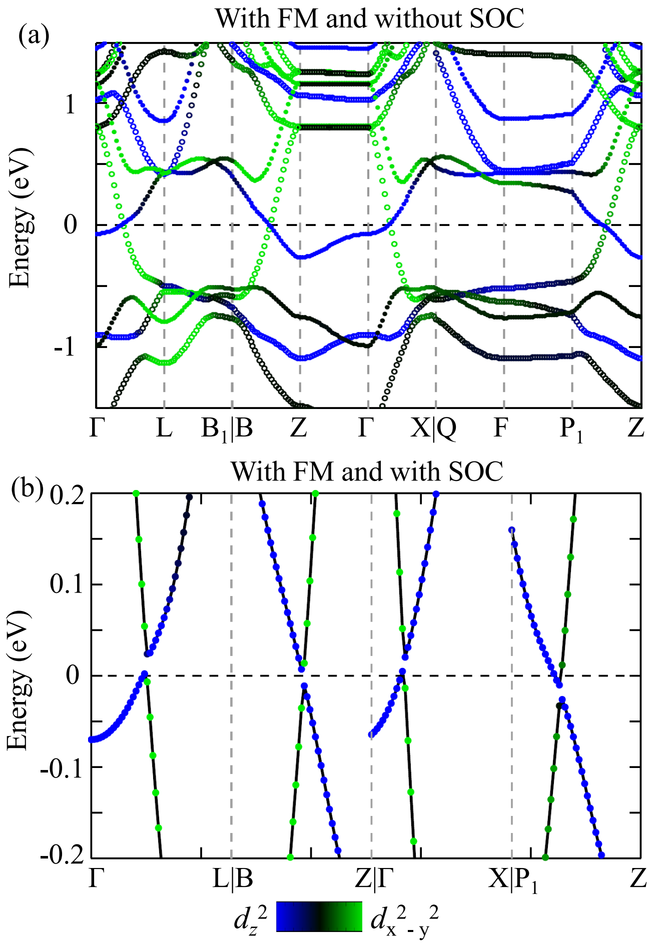

FIG. 2. (Color online) (a) Band structure of LaBr in the FM state without SOC. The horizontal dashed line gives the Fermi level. Blue and green colors indicate d_{z^2} and $d_{x^2-y^2}$ orbitals weight of the La atoms, while the black color is the weight of the other orbitals. Open and filled symbols represent spin-up and spin-down states, respectively. (b) Low-energy view of the same band structure, but with SOC and plotted only along representative directions where the band gap opens across the Fermi level. The overall band structure at other directions and higher energy is similar to that of (a). Black solid lines are the guide to the eyes, where symbols are the calculated points.

Since the Weyl ring occurs between different spin states from different orbitals, as the SOC is turned on, all k points on the Weyl rings become gapped, and the system enters into an insulator state [see Fig. 2(b), and Ref. [46] for 2D band plots and density of states). We obtain a band gap of 14 meV for LaCl, 22 meV for LaBr, and 25 meV for LaI without tuning. Tiny semimetallic Fermi pockets are present for the calculations with relaxed lattice structure, which are lifted from E_{F} with small strain (see Fig. 5). With strain and/or pressure, the insulating band gap can be enhanced to above 75 meV. As the band gap opens at the inverted bands crossing points via SOC, a QAH effect can be expected in such systems.

B. Tight-binding Hamiltonian and Berry phase computation

Guided by the DFT band structure, we derive a realistic tight-binding model by including the two low-lying e_g orbitals. The FM ordering is introduced by the mean-field Heisenberg term, in which we allow exchange couplings to be orbital dependent (J_1, J_2). The interorbital SOC is restricted to be nearest neighbor, which turns out to have a form of $\lambda_k = \lambda(\sin k_x + i \sin k_y)$, where λ is the SOC coupling strength. Two adjacent La layers are inequivalent (denoted by A and B), in which each La atom is surrounded by six other La atoms in a hexagonal plane, and three La atoms in a trigonal plane are placed at $\sim c/10$ distance along the z axis [see Fig. 1(a). If we set our multiband spinor for each layer as $\psi_k^{A/B} = (|d^{\uparrow}_{x^2-y^2}\rangle, |d^{\uparrow}_{z^2}\rangle, |d^{\downarrow}_{x^2-y^2}\rangle, |d^{\downarrow}_{z^2}\rangle)$, the bulk Hamiltonian can then be expressed as $H_A(k) =$

$$\begin{pmatrix} \xi_{1k} + J_1 m & \xi_{3k} & 0 & \lambda_k \\ \xi_{3k}^* & \xi_{2k} - J_2 m & \lambda_k & 0 \\ 0 & \lambda_k^* & \xi_{1k} - J_1 m & \xi_{3k} \\ \lambda_k^* & 0 & \xi_{3k}^* & \xi_{2k} + J_2 m \end{pmatrix}. \quad (1)$$

For the lattice structure depicted in Fig. 1, we obtain the noninteracting dispersions ξ_{jk} for both the intra- (j=1, 2) and interorbitals ($j = 3$) as $\xi_{jk} = 2t_j^1 \cos k_x a + 4t_j^2 \cos \frac{k_x a}{2} \cos \frac{\sqrt{3} k_y a}{2} - \mu_j$. Here t_j^i are the nearest-neighbor, tight-binding hopping parameters for the ith orbital. $\mu_1 = \mu$ is the chemical potential, $\mu_2 = \mu + \Delta$, including both the chemical potential and the on-site energy difference between two orbitals, and $\mu_3 = 0$. a and c are the in-plane and out-of-plane lattice constants. Due to symmetry considerations, the Hamiltonian for the B plane is $H_B = H_A$. Finally, nearest-neighbor hopping terms between the A and B layers turn out to be

$$\xi_{jk}^{AB} = t_j^3 e^{-i(\frac{k_y a}{\sqrt{3}} + \frac{k_z c}{10})} + 2t_j^4 \cos \frac{k_x a}{2} e^{i(\frac{k_y a}{2\sqrt{3}} - \frac{k_z c}{10})}. \quad (2)$$

Here also, j stands for the same intra- ($j = 1,2$) and interorbital ($j = 3$) hoppings. The parameter values are deduced by fitting to the DFT dispersion as shown in Fig. 3(a). Our fitting yields $J_1 = –0.43$ eV, $J_2 = –0.69$ eV, and $\lambda = 20$ meV, which are close to the DFT values listed above. The other parameters are given in Appendix B. The overall fitting is reasonably good, and the tight-binding band structure captures the important topological properties including band inversion, the nodal Weyl ring, and the insulating gap formation with SOC in accordance with the DFT calculation.

IV. TOPOLOGICAL PROPERTIES OF LA*X*

A. Berry curvature and Chern number

Near the Weyl ring, the same Hamiltonian can be reduced to that of the topological insulator Hamiltonian [6]. Since band inversion has already occurred between opposite spin states, the SOC-induced insulating gap renders QAH insulators [12,14]. Due to the quasi-2D nature of the La bilayers, the topological invariant for the QAH can be estimated from the Berry connection [12,14,51]. We have computed Berry curvature, $\Omega(k_x,k_y)$, at constant k_z by using the Kubo formula:

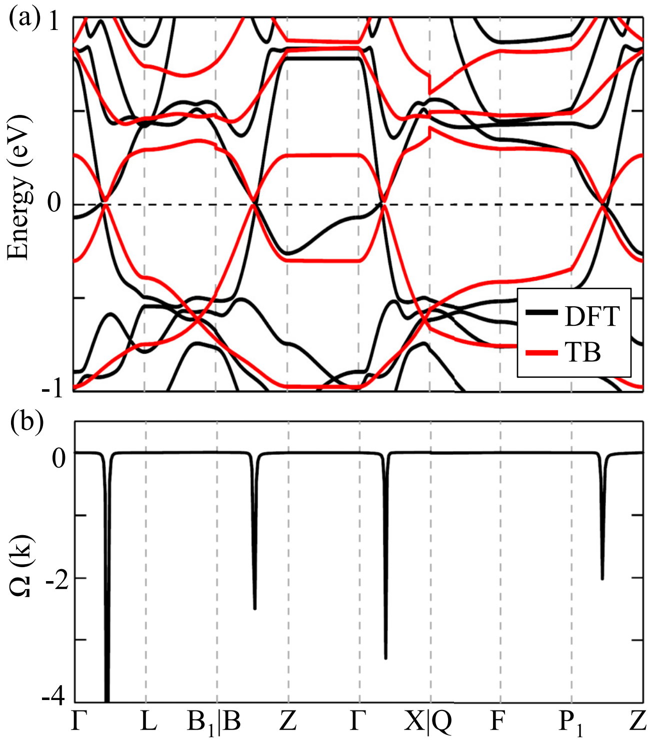

FIG. 3. (Color online) (a) Tight-binding band structure (red lines), overlayed on top of the DFT band structure (black lines) of LaBr with FM order and SOC. (b) Computed Berry curvature along the same high-symmetry directions as in (a), exhibiting spikes at the momenta where SOC gaps the FM Weyl points.

$$\Omega(k) = \hbar^2 \sum_{n \neq n'} \frac{\mathrm{Im}[\langle nk|v_x|n'k\rangle\langle n'k|v_y|nk\rangle]}{(E_{nk} - E_{n'k})^2} \times [n_f(E_{nk}) - n_f(E_{n'k})]. \quad (3)$$

Here v_x and v_y are velocity operators in the x and y directions, respectively, defined as $v_x = \frac{1}{\hbar}\frac{\partial H}{\partial k_x}$ and $v_y = \frac{1}{\hbar}\frac{\partial H}{\partial k_y}$. $\frac{\partial H}{\partial k_{x/y}}$ represents a derivative of each element of the Hamiltonian matrix. $|nk\rangle$ and $|n'k\rangle$ are eigenvectors of H with eigenvalues E_{nk} and $E_{n'k}$, respectively, and $n_f(E_{nk})$ is the Fermi occupation number at energy E_{nk}. The obtained Berry curvature is plotted along the representative high-symmetry directions (for different directions, the corresponding k_z values are kept constant), in Fig. 3(c) along the high-symmetry directions. $\Omega(\mathbf{k})$ exhibits a strong spikelike anomaly at the gapped Weyl points, signaling the presence of a Hall plateau [12].

Finally, we calculate the Hall conductance σ_{xy} which is related to the Chern number C by $\sigma_{xy} = C\frac{e}{h^2}$, where the Chern number C is given by

$$C = \frac{1}{2\pi}\int_{BZ} \Omega(k) d^2k. \quad (4)$$

Each two-dimensional (2D) La layer constitutes a hexagon. The Chern number is calculated by summing the Berry curvature on each k_z plane, which comes out to be -1, signaling the presence of a QAH effect. The result is valid

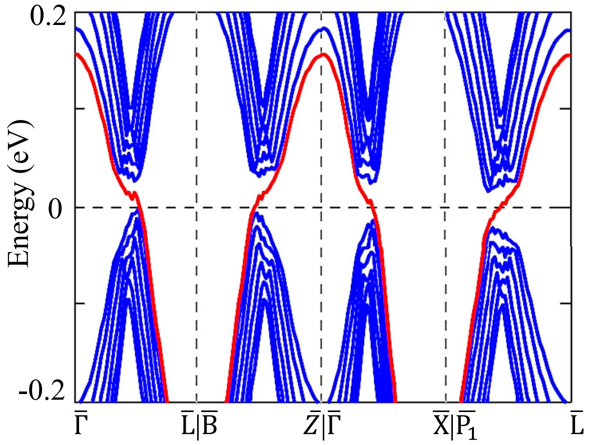

FIG. 4. (Color online) Edge states (red lines) along representative high-symmetry directions where SOC opens a gap in Fig. 2(b).

even in the semimetallic state, as long as the Fermi surface pocket is small enough, and a single-valued Chern number can be defined for the filled bands.

B. Edge state

We also calculate the edge state for various representative cuts and the results are shown in Fig. 4. For all cases, we have used eight La bilayers, and the cut is chosen in such a way that the direction of plotting is fully periodic while the perpendicular direction has open boundary conditions. For example, along the $\bar{\Gamma} \rightarrow \bar{L}$ direction, we have made the supercell along the b direction, with k_x and k_z remaining the good quantum number. Similar consideration is taken for all other directions. We find that the magnetically polarized edge state adiabatically connects both the bulk valence and conducting bands, following the topological criterion of the QAH state [5–7].

V. STRAIN ENGINEERING AND BAND-GAP ENHANCEMENT

Strain is a straightforward and efficient method to tune the band gap. We find that uniaxial strain can increase the band gap of LaBr and LaCl systems up to two to three times its value in the relaxed coordinates. Moreover, only a very small amount of strain is necessary to remove the states from E_F at all momenta, as shown in Fig. 5(a) for 0.24% strain in LaBr. The full strain dependence of the band gap is plotted in Fig. 5(b). It is interesting to see that the band gap of LaBr increases rapidly for very small positive strain, without undergoing any structural transition. For LaCl, the band-gap tuning is very much monotonic with strain. On the other hand, LaI does not exhibit any considerable band-gap change for this range of strain; presumably due to the large ionic size of the I atom the effect of strain is reduced here. A comprehensive list of various QAH systems, their tuning mechanism, and the corresponding gap values is provided in Table I. In comparison to the existing materials, which all require some sort of tuning to obtain the QAH state, the present systems are not only intrinsic QAH insulators, but also provide an opportunity to obtain larger band gaps than most of the earlier systems.

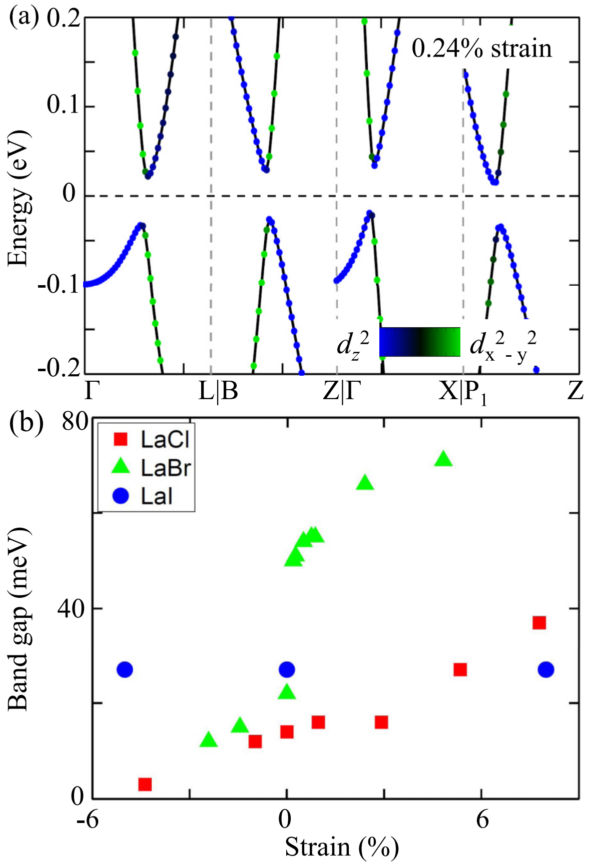

FIG. 5. (Color online) Strain engineering and band-gap tuning. (a) Insulating band structure of LaBr in the FM + SOC state with only 0.24% uniaxial strain. (b) Strain-induced band-gap evolution for all three QAH systems.

VI. CONCLUSION

Our prediction will help realize the long-sought goal where the QAH effect can be realized and utilized in single crystals. Moreover, the predicted band gap is large enough for many practical and experimental purposes, and larger than most of the earlier predicted systems. The layered structures of LaX compounds are easy to cleave to obtain topological surface states. These advantages will allow full access to the thermal and electric transport regime of the QAH edge states without having the problem of magnetic impurity or thin-film growth. Furthermore, this work will accelerate the prediction and discovery of more intrinsic QAH insulators within the lanthanides and beyond.

Diverse other possibilities can be explored in intrinsic QAH insulators with long-ranged FM ordering. Goldstone mode, a collective zero-energy magnetic excitation, is a natural consequence of the continuous symmetry breaking, which can be expected to evolve with topological consequences in the QAH insulator [52]. Chiral spin current in the edge state can lead to Skyrmion excitations [53]. Owing to the heavy electron mass of La electrons, other rare-earth substitutions in the La site can bring in Kondo physics, a mixed valence state within the topological matrix. The surface states of the QAH insulator are also a potential host of axion particles [54].

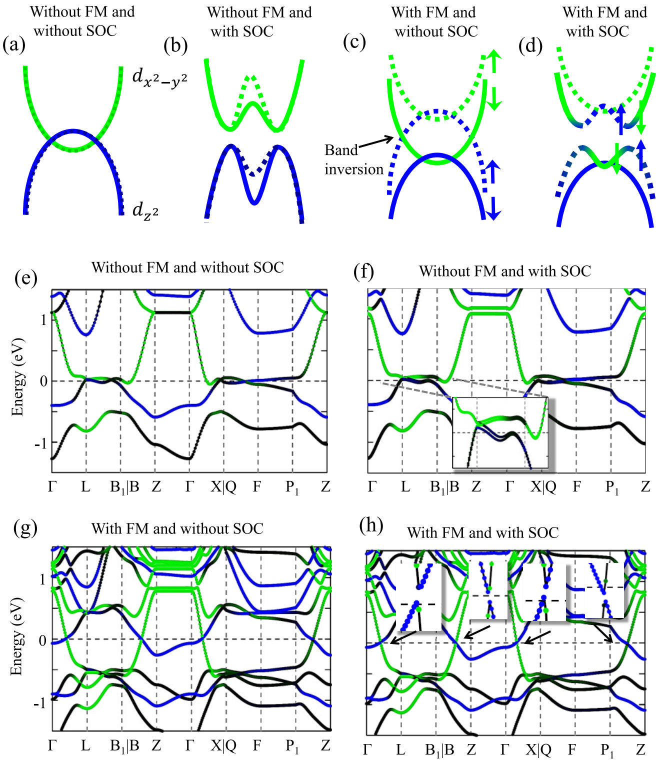

FIG. 6. (Color online) Band progression of LaX materials. (a–d) The upper panel schematically illustrates the band structure around the band crossings between two different orbitals near the Fermi level for four different cases. (a) Band structure in the absence of FM order and SOC. (c) Same as (a) but with SOC. This particular example is representative of the LaX materials where SOC splitting can be anisotropic across the band crossing points. (c) Bands with FM order and without SOC. (c) Once SOC is included, an insulating gap forms between different orbitals and spins. (e–h) DFT band structure for the four cases discussed in the upper panels in the same order. Various insets highlight the low-energy regions where SOC induces a band gap.

ACKNOWLEDGMENT

This work is facilitated by the Bardeen HPC cluster facility in the Physics Department of the Indian Institute of Science.

APPENDIX A: FULL BAND PROGRESSION WITH AND WITHOUT SOC OR FM ORDER

In Fig. 6 we give the details of the band progression of LaBr, with and without SOC and FM. Here the band crossing and band inversion occur at non-high-symmetric k points, and thus undergo band splitting due to SOC, even in the presence of time-reversal and inversion symmetries. This is demonstrated from the DFT calculation as well in Fig. 6(f). In the FM state, the majority and minority bands from different orbitals cross each other at the Fermi level, which in fact sets the stage for the band inversion and insulating gap when SOC is turned on. The band crossings occur at a contour of k points, which all become gapped with SOC and a fully insulating gap indeed opens in these systems. The 2D band plots at various k_z cuts as well as density of states are shown in Ref. [46].

APPENDIX B: FURTHER DETAILS OF THE TIGHT-BINDING MODEL

Here we expand the description of the tight-binding (TB) model. First we describe the nonmagnetic state, then the effect of magnetism is considered within a mean-field treatment, and finally the SOC is included. The TB parameters are obtained by fitting the band structure to the corresponding DFT calculation. The structure of LaBr is given by two layers of 2D hexagonal lattices stacked along the c direction, as shown in Fig. 1. The in-plane TB Hamiltonian therefore remains the same for each layer, and we have only considered the nearest-neighbor interlayer hopping:

$$H = \begin{bmatrix} H_A & H_{AB} \\ H^*_{AB} & H_B \end{bmatrix}. \tag{B1}$$

If we choose our origin of reference at the center of the hexagon (point A) in Fig. 1(b), then the coordinates of nearest-neighbor lattice points are given by

$$\mathrm{A} \equiv (0,0,0), \qquad \mathrm{B} \equiv (a,0,0), \qquad \mathrm{C} \equiv \left(\frac{a}{2},\frac{\sqrt{3}a}{2},0\right),$$

$$\mathrm{D} \equiv \left(-\frac{a}{2},\frac{\sqrt{3}a}{2},0\right), \qquad \mathrm{E} \equiv (-a,0,0),$$

$$\mathrm{F} \equiv \left(-\frac{a}{2},-\frac{\sqrt{3}a}{2},0\right), \qquad \mathrm{G} \equiv \left(\frac{a}{2},-\frac{\sqrt{3}a}{2},0\right),$$

$$\mathrm{H} \equiv \left(0,-\frac{\sqrt{3}a}{3},-\frac{c}{10}\right), \qquad \mathrm{I} \equiv \left(\frac{a}{2},\frac{\sqrt{3}a}{6},-\frac{c}{10}\right),$$

$$\mathrm{J} \equiv \left(-\frac{a}{2},\frac{\sqrt{3}a}{6},-\frac{c}{10}\right).$$

The effective two-orbital Hamiltonian for each layer (say, the A layer) is given by

$$H_A = \sum_{k,i=1,2,\sigma} \xi_{ik} c^\dagger_{ik\sigma} c_{ik\sigma} + \sum_{k,\sigma} \xi_{3k} c^\dagger_{1k\sigma} c_{2k\sigma} + \sum_{k,i,\alpha,\beta} J_i m c^\dagger_{ik\alpha} \sigma^z_{\alpha\beta} c_{ik\beta} + \sum_{k,i,j\neq i,\alpha,\beta\neq\alpha} \lambda_k c^\dagger_{ik\alpha} c_{jk\beta}, \tag{B2}$$

where $c_{jk\sigma}$ is the destruction operator for the jth orbital ($j = 1$ for $d_{x^2-y^2}$ and 2 for d_{z^2} orbital), k is the crystal momentum index, and σ is the spin index, which can take two values as ↑ for up-spin and ↓ for down-spin. The first term of the Hamiltonian represents intraorbital hopping; the second term is the interorbital hopping; the third term is the Heisenberg term; and the last one is the SOC term. ξ_{ik} are intraorbital band dispersions for $d_{x^2-y^2}$ and d_{z^2} orbitals, respectively, and ξ_{3k} is the interorbital band dispersion. J_i are Heisenberg couplings, and m is spontaneous magnetization. σ^z is the third Pauli matrix, and λ_k is the nearest-neighbor SOC.

In the TB model only nearest-neighbor hoppings are considered. For a single layer each lattice site has six nearest neighbors at the vertices of the hexagon surrounding the lattice site. Also, due to the similar spatial symmetry of the two e_g orbitals considered here, phase differences between different sites for the two orbitals come out to be the same, except TB hopping parameters. For simplicity, we define all TB parameters as t_j^i, where the subscript j denotes different orbitals ($j = 1$ and 2 for two intraorbital terms, and 3 for the interorbital term), while the superscript i differentiates them for different sites. Hopping from site A to site B yields $t_j^1 e^{i\mathbf{k}(\mathbf{r}_\mathrm{B}-\mathbf{r}_\mathrm{A})} = t_j^1 e^{ik_x a}$, where $\mathbf{r}_\mathrm{A}$ and $\mathbf{r}_\mathrm{B}$ are the positions of A and B sites, and "a" is the in-plane lattice constant. All TB parameters for hoppings to C, D, F, and G sites from site A are equal to each other as the distances are the same, and we denote it by t_j^2. Therefore, the in-plane dispersion for both intra- and interorbitals becomes

$$\begin{aligned}\xi_{jk} &= t_j^1[e^{ik_x a} + e^{-ik_x a}] + t_j^2\Big[\big\{e^{i(k_x\frac{a}{2}+k_y\frac{\sqrt{3}a}{2})} + e^{-i(k_x\frac{a}{2}+k_y\frac{\sqrt{3}a}{2})}\big\}\\ &\quad + \big\{e^{i(k_x\frac{a}{2}-k_y\frac{\sqrt{3}a}{2})} + e^{-i(k_x\frac{a}{2}-k_y\frac{\sqrt{3}a}{2})}\big\}\Big] - \mu_j,\\ &= 2t_j^1 \cos k_x a + 4t_j^2 \cos\frac{k_x a}{2}\cos\frac{\sqrt{3}k_y a}{2} - \mu_j. \end{aligned} \tag{B3}$$

The last term μ_j encodes various contributions: Let us say $\mu_1 = \mu$ is the chemical potential of the system, then $\mu_2 = \mu + \Delta$, where Δ is the on-site energy difference of the second orbital from the first one. Since the interorbital hopping involves neither an on-site term, nor the chemical potential, so $\mu_3 = 0$. For intraorbital hopping of the d_{z^2} orbital, due to its azimuthal symmetry, both TB parameters are the same, i.e., $t_2^1 = t_2^2$.

Now we consider the Hamiltonian for layer B. It is easily recognized from the structure that layer B and layer A are the same. We set $H_A(k) = H_B(k)$. Next we derive the Hamiltonian for interlayer dispersion ξ_{jk}^{AB}. The distance between the A and B layers is about $c/10$. The nearest-neighbor sites to the A atom are H, I, and J. By doing a similar algebra as for the planer dispersion, we obtain the bare dispersions for the interlayer terms as

$$\xi_{jk}^{AB} = t_j^3 e^{-i(\frac{k_y a}{\sqrt{3}}+\frac{k_z c}{10})} + 2t_j^4\cos\left(\frac{k_x a}{2}\right)e^{i(\frac{k_y a}{2\sqrt{3}}-\frac{k_z c}{10})}. \tag{B4}$$

For the same azimuthal symmetry of the the d_{z^2} orbital, $t_2^3 = t_2^4$.

If we choose the basis of our wave function for each layer ψ_k^A as $\psi_k^A = (c_{1k\uparrow} c_{2k\uparrow} c_{1k\downarrow} c_{2k\downarrow})$, then the corresponding Hamiltonian can be expressed in a 4×4 matrix (and 8×8 matrix for two layers) as $H_A(k) = \langle\psi_k^A|H|\psi_k^A\rangle$. We include SOC in the present lattice as evaluated by Haldane [3] to be $\lambda_k = \lambda(\sin k_x + i \sin k_y)$. Therefore, by including the FM order and the SOC, we get the final Hamiltonian for the intralayer (A) as $H_A(k) =$

$$\begin{bmatrix} \xi_{1k} + J_1 m & \xi_{3k} & 0 & \lambda_k \\ \xi_{3k}^* & \xi_{2k} - J_2 m & \lambda_k & 0 \\ 0 & \lambda_k^* & \xi_{1k} - J_1 m & \xi_{3k} \\ \lambda_k^* & 0 & \xi_{3k}^* & \xi_{2k} + J_2 m \end{bmatrix}, \tag{B5}$$

and for the interlayer as

$$H_{AB}(k) = \begin{bmatrix} \xi_{1k}^{AB} & \xi_{3k}^{AB} & 0 & 0 \\ \xi_{3k}^{AB*} & \xi_{2k}^{AB} & 0 & 0 \\ 0 & 0 & \xi_{1k}^{AB} & \xi_{3k}^{AB} \\ 0 & 0 & \xi_{3k}^{AB*} & \xi_{2k}^{AB} \end{bmatrix}. \tag{B6}$$

The eigenvalues of the 8×8 Hamiltonian give energy dispersions. We have fitted the energy bands obtained from our model to DFT bands, and the values of the parameters are the following (in electronvolts): $t_1^1 = -0.0553$, $t_1^2 = -0.0597$, $\mu_1 = -1.2345$, $t_2^1 = t_2^2 = 0.037$, $\mu_2 = -0.0662$, $t_3^1 = 0.0522$, $t_3^2 = 0.0499$, $t_1^3 = 0.4471$, $t_1^4 = -0.0776$, $t_2^3 = t_2^4 = 0.177$, $t_3^3 = -0.1904$, $t_3^4 = -0.045$, $m = 0.8$, $J_1 = -0.4251$, $J_2 = -0.6927$, and $\lambda = 0.02$.

The TB bands fit well to the DFT bands in the regions where the corresponding weights of the $d_{x^2-y^2}$ and d_{z^2} orbitals are dominant. When we include the effect of magnetization but no SOC (i.e., J_i are finite, $\lambda = 0$), each energy band splits into two magnetic bands, and there are crossings of bands at a contour of momentum, reproducing the nodal Weyl ring. This signals the presence of a band inversion in the FM states. Once the SOC is turned on (i.e., both J_i and λ are finite), an inverted band gap opens at the band crossing points.

[1] K. V. Klitzing, G. Dorda, and M. Pepper, Phys. Rev. Lett. **45**, 494 (1980).

[2] D. J. Thouless, M. Kohmoto, M. P. Nightingale, and M. den Nijs, Phys. Rev. Lett. **49**, 405 (1982).

[3] F. D. M. Haldane, Phys. Rev. Lett. **61**, 2015 (1988).

[4] B. I. Halperin, Phys. Rev. B **25**, 2185 (1982).

[5] M. Z. Hasan and C. L. Kane, Rev. Mod. Phys. **82**, 3045 (2010).

[6] X.-L. Qi and S.-C. Zhang, Rev. Mod. Phys. **83**, 1057 (2011).

[7] A. Bansil, H. Lin, and T. Das [Rev. Mod. Phys. (to be published)].

[8] J. K. Jain, Phys. Rev. Lett. **63**, 199 (1989).

[9] M. König, S. Wiedmann, C. Brüne, A. Roth, H. Buhmann, L. W. Molenkamp, X.-L. Qi, and S.-C. Zhang, Science **318**, 766 (2007).

[10] C.-Z. Chang, J. Zhang, X. Feng, J. Shen, Z. Zhang, M. Guo, K. Li, Y. Ou, P. Wei, L.-L. Wang *et al.*, Science **340**, 167 (2013).

[11] C.-Z. Chang, W. Zhao, D. Y. Kim, H. Zhang, B. A. Assaf, D. Heiman, S.-C. Zhang, C. Liu, M. H. W. Chan, and J. S. Moodera, Nat. Mater. **14**, 473 (2015).

[12] Z. Qiao, W. Ren, H. Chen, L. Bellaiche, Z. Zhang, A. H. MacDonald, and Q. Niu, Phys. Rev. Lett. **112**, 116404 (2014).

[13] G. Xu, H. Weng, Z. Wang, X. Dai, and Z. Fang, Phys. Rev. Lett. **107**, 186806 (2011).

[14] R. Yu, W. Zhang, H.-J. Zhang, S.-C. Zhang, X. Dai, and Z. Fang, Science **329**, 61 (2010).

[15] C.-X. Liu, X.-L. Qi, X. Dai, Z. Fang, and S.-C. Zhang, Phys. Rev. Lett. **101**, 146802 (2008).

[16] K. Dolui and T. Das, arXiv:1412.2607.

[17] Z. Qiao, S. A. Yang, W. Feng, W. K. Tse, J. Ding, Y. Yao, J. Wang, and Q. Niu, Phys. Rev. B **82**, 161414 (2010).

[18] J. Ding, Z. Qiao, W. Feng, Y. Yao, and Q. Niu, Phys. Rev. B **84**, 195444 (2011).

[19] H. Zhang, C. Lazo, S. Blügel, S. Heinze, and Y. Mokrousov, Phys. Rev. Lett. **108**, 056802 (2012).

[20] X.-L. Zhang, L.-F. Liu, and W.-M. Liu, Sci. Rep. **3**, 2908 (2013).

[21] T. P. Kaloni, N. Singh, and U. Schwingenschlögl, Phys. Rev. B **89**, 035409 (2014).

[22] M. Ezawa, Phys. Rev. Lett. **109**, 055502 (2012).

[23] X. Kou, M. Lang, Y. Fan, Y. Jiang, T. Nie, J. Zhang, W. Jiang, Y. Wang, Y. Yao, L. He, and K. L. Wang, ACS Nano **7**, 9205 (2013).

[24] C. Niu, Y. Dai, L. Yu, and B. Huang, Appl. Phys. Lett. **102**, 092402 (2013).

[25] K. F. Garrity and D. Vanderbilt, Phys. Rev. Lett. **110**, 116802 (2013).

[26] K. F. Garrity and D. Vanderbilt, Phys. Rev. B **90**, 121103 (2014).

[27] Z. F. Wang, Z. Liu, and F. Liu, Phys. Rev. Lett. **110**, 196801 (2013).

[28] H. Zhang, Y. Xu, J. Wang, K. Chang, and S.-C. Zhang, Phys. Rev. Lett. **112**, 216803 (2014).

[29] A. M. Cook and A. Paramekanti, Phys. Rev. Lett. **113**, 077203 (2014).

[30] H. Zhang, H. Huang, K. Haule, and D. Vanderbilt, Phys. Rev. B **90**, 165143 (2014).

[31] K.-Y. Yang, W. Zhu, D. Xiao, S. Okamoto, Z. Wang, and Y. Ran, Phys. Rev. B **84**, 201104(R) (2011).

[32] F. Wang and Y. Ran, Phys. Rev. B **84**, 241103 (2011).

[33] X. Hu, A. Rüegg, and G. A. Fiete, Phys. Rev. B **86**, 235141 (2012).

[34] C. Fang, M. J. Gilbert, and B. A. Bernevig, Phys. Rev. Lett. **112**, 046801 (2014).

[35] H. Lin, L. A. Wray, Y. Xia, S. Xu, S. Jia, R. J. Cava, A. Bansil, and M. Z. Hasan, Nat. Mater. **9**, 546 (2010).

[36] S. Chadov, X. Qi, J. Kübler, G. H. Fecher, C. Felser, and S. C. Zhang, Nat. Mater. **9**, 541 (2010).

[37] R. von Helmolt, J. Wecker, B. Holzapfel, L. Schultz, and K. Samwer, Phys. Rev. Lett. **71**, 2331 (1993).

[38] R. Scherwitzl *et al.*, Appl. Phys. Lett. **95**, 222114 (2009).

[39] J. G. Bednorz and K. A. Müller, Z. Phys. B: Condens. Matter **64**, 189 (1986).

[40] J. P. Perdew, K. Burke, and M. Ernzerhof, Phys. Rev. Lett. **77**, 3865 (1996).

[41] G. Kresse and J. Furthmüller, Phys. Rev. B **54**, 11169 (1996).

[42] G. Kresse and D. Joubert, Phys. Rev. B **59**, 1758 (1999).

[43] D. Aberg, B. Sadigh, and P. Erhart, Phys. Rev. B **85**, 125134 (2012).

[44] J. Klimes, D. R. Bowler, and A. Michaelides, Phys. Rev. B. **83**, 195131 (2011).

[45] A. V. Krukau, O. A. Vydrov, A. F. Izmaylov, and G. E. Scuseria, J. Chem. Phys. **125**, 224106 (2006).

[46] See Supplemental Material at http://link.aps.org/supplemental/10.1103/PhysRevB.92.205133 for various details and further results.

[47] A. Togo, F. Oba, and I. Tanaka, Phys. Rev. B **78**, 134106 (2008).

[48] M. Phillips and V. Aji, Phys. Rev. B **90**, 115111 (2014).

[49] Y. Kim, B. J. Wieder, C. L. Kane, and A. M. Rappe, Phys. Rev. Lett. **115**, 036806 (2015).

[50] K. Mullen, B. Uchoa, and D. T. Glatzhofer, Phys. Rev. Lett. **115**, 026403 (2015).

[51] X. Wang, J. R. Yates, I. Souza, and D. Vanderbilt, Phys. Rev. B **74**, 195118 (2006).

[52] R. Nandkishore and L. Levitov, Phys. Rev. B **82**, 115124 (2010).

[53] M. Onoda, G. Tatara, and N. Nagaosa, J. Phys. Soc. Jpn. **73**, 2624 (2004).

[54] R. Li, J. Wang, X.-L. Qi, and S. C. Zhang, Nat. Phys. **6**, 284 (2010).